

## *Retraction*

# **Retracted: Analysis of VLF Wave Field Components and Characteristics Based on Finite Element Time-Domain Method**

### **Journal of Sensors**

Received 19 December 2023; Accepted 19 December 2023; Published 20 December 2023

Copyright © 2023 Journal of Sensors. This is an open access article distributed under the Creative Commons Attribution License, which permits unrestricted use, distribution, and reproduction in any medium, provided the original work is properly cited.

This article has been retracted by Hindawi following an investigation undertaken by the publisher [1]. This investigation has uncovered evidence of one or more of the following indicators of systematic manipulation of the publication process:

- (1) Discrepancies in scope
- (2) Discrepancies in the description of the research reported
- (3) Discrepancies between the availability of data and the research described
- (4) Inappropriate citations
- (5) Incoherent, meaningless and/or irrelevant content included in the article
- (6) Manipulated or compromised peer review

The presence of these indicators undermines our confidence in the integrity of the article's content and we cannot, therefore, vouch for its reliability. Please note that this notice is intended solely to alert readers that the content of this article is unreliable. We have not investigated whether authors were aware of or involved in the systematic manipulation of the publication process.

Wiley and Hindawi regrets that the usual quality checks did not identify these issues before publication and have since put additional measures in place to safeguard research integrity.

We wish to credit our own Research Integrity and Research Publishing teams and anonymous and named external researchers and research integrity experts for contributing to this investigation.

The corresponding author, as the representative of all authors, has been given the opportunity to register their agreement or disagreement to this retraction. We have kept a record of any response received.

### **References**

- [1] Q. Wang, H. Zhu, Z. Chai, Z. Cui, and Y. Wang, "Analysis of VLF Wave Field Components and Characteristics Based on Finite Element Time-Domain Method," *Journal of Sensors*, vol. 2023, Article ID 7702342, 15 pages, 2023.

## Research Article

# Analysis of VLF Wave Field Components and Characteristics Based on Finite Element Time-Domain Method

Qile Wang <sup>1</sup>, Hanhao Zhu <sup>1,2</sup>, Zhigang Chai,<sup>3</sup> Zhiqiang Cui,<sup>3</sup> and Yafen Wang<sup>4</sup>

<sup>1</sup>Institute of Marine Science and Technology, Zhejiang Ocean University, Zhoushan 316022, China

<sup>2</sup>Donghai Laboratory, Zhoushan, Zhejiang 316021, China

<sup>3</sup>School of Naval Architecture and Maritime, Zhejiang Ocean University, Zhoushan 316022, China

<sup>4</sup>Unit 91977 of the People's Liberation Army, Beijing 150001, China

Correspondence should be addressed to Hanhao Zhu; [zhuhanhao@zjou.edu.cn](mailto:zhuhanhao@zjou.edu.cn)

Received 8 August 2022; Revised 20 September 2022; Accepted 3 October 2022; Published 26 April 2023

Academic Editor: Yuan Li

Copyright © 2023 Qile Wang et al. This is an open access article distributed under the Creative Commons Attribution License, which permits unrestricted use, distribution, and reproduction in any medium, provided the original work is properly cited.

Most traditional sound field calculation methods regard the seabed as the horizontal stratified liquid sea bottom and conduct simulation analysis based on the frequency domain. Hence, the generality of the above research methods is limited to varying degrees. To accurately clarify the propagation characteristics and mechanism of very low-frequency (VLF,  $\leq 100$  Hz) sound waves in the shallow sea, a numerical calculation model is established using the finite element time-domain method (FETD) based on the three-dimensional cylindrical coordinate system. Using this model, the effects of sea-bottom topographies and geoacoustic parameters on the composition and characteristics of VLF sound fields in the shallow sea and their corresponding mechanism are investigated through the comparative analysis of various numerical simulation examples. The simulation results demonstrate that the low-frequency sound field in the full waveguide of the shallow sea is composed of normal mode waves in the seawater layer, Scholte waves at the liquid-solid interface, and elastic waves at the sea bottom. Compared with the soft sea bottom, which has a more negligible elastic impedance, the hard sea bottom is more conducive to the long-distance propagation of normal mode waves and the excitation of Scholte waves. The Scholte waves on the hard sea bottom are significantly stronger than those on the soft sea bottom. Compared with the horizontal sea bottom, the uphill topography enhances the sound energy leakage to the sea bottom. It is more favorable to receive Scholte waves at shallow depths, whereas the influence laws of downhill topography are the opposite.

## 1. Introduction

Numerical calculation of sound propagation mechanism in the shallow sea has always been an important research topic in ocean acoustics [1, 2]. After 50 to 60 years of research, several acoustic field numerical calculation methods have been developed, such as the normal mode method, ray method, parabolic equation method, fast field method, and their derivative methods [3–7]. However, these methods mainly calculate sound propagation characteristics in the frequency domain, for example, the transmission loss and frequency response of underwater acoustic energy in seawater. At the same time, the sea bottom is treated as a liquid medium with horizontal stratification during calculations [6–8]. In reality, the shallow sea is generally a complex ocean

environment with an elastic sea bottom that is not horizontally stratified. The current research results demonstrate that the geoacoustic parameters and topography of the sea bottom significantly influence low-frequency sound propagation in a shallow sea [7]. Therefore, the above research methods cannot meet the actual shallow sea sound field calculation needs.

Due to the development of submarine stealth technology and the requirements for monitoring various physical ocean phenomena, the detection methods for targets in shallow water gradually turn to very low frequency (VLF,  $\leq 100$  Hz) [9]. VLF acoustic signals with strong penetrating power penetrate the sea bottom when propagating in the shallow sea. Thus, VLF acoustic energy leaks into the sea bottom and excites other sound field components that can propagate

through the sea bottom or liquid-solid interface [10–13]. These components—such as the compression wave (P-waves), the shear wave (S-waves), the normal mode waves, and the interface waves—are all important for understanding the conversion mechanism and spatial and temporal distribution of low-frequency sound waves [13–16]. The systematic study of excitation, propagation, and detection of different components of low-frequency sound fields has essential application value in ocean acoustics and geophysics. However, these components cannot be distinguished accurately in the frequency domain. The previous research focused on the seawater layer and could not give the variation characteristics of the acoustic energy in the seabed layer. To achieve the research goal, a numerical calculation of the VLF sound field in shallow seas needs to be conducted in the time domain with a full waveguide model. Then, the mechanism and characteristics of different components of the VLF sound field can be analyzed accurately.

The finite element method discretizes a physical field into limited units and then establishes finite linear equations using the connections between these units to obtain the exact solutions of the physical field [17–19]. Therefore, the finite element method is more suitable for deriving an accurate solution of sound fields in complex ocean environments. However, due to the large amount of calculation effort required in processing, the finite element method has rarely been applied to the calculation of large-scale ocean sound field models in the past, except for providing reference solutions [20]. With the advances in computer technology, it is now possible to support the application of the finite element method in calculating shallow sea sound fields. Based on the above research status, we have proposed a time-domain numerical calculation model for investigating various wave components of the full waveguide sound field using the finite element time-domain method (FETD). Using this model, the effects of different sea-bottom geoacoustic parameters and topographies on the low-frequency sound field composition and characteristics are simulated and analyzed. The results of this work may provide theoretical guidance for ocean sound field modeling analysis and prediction.

In Section 2, the method based on FETD for calculating the full waveguide sound field is described. In Section 3, the accuracy of this model is verified by comparing the experimental results with the existing calculation results. In Section 4, the effects of sea-bottom geoacoustic parameters and topographies on VLF sound fields composition and propagation mechanism are elaborated by the comparative analysis of various numerical examples. Finally, Section 5 briefly summarizes this study's research emphases and conclusions.

## 2. Theoretical Model

This section describes the full waveguide model for shallow sea, based on the three-dimensional cylindrical coordinate system  $(r, \theta, z)$ , and the  $N \times 2D$  hypothesis is described. Therefore, acoustic wave coupling in the  $\theta$  direction of adjacent two-dimensional vertical planes is neglected [21]. As shown in Figure 1, the  $z$ -axis indicates the depth of the sea and the plane  $z = 0$  means the sea surface. The  $r$ -axis repre-

sents the direction of the horizontal propagation of the acoustic signals,  $V_w$  is defined as the seawater layer,  $V_b$  is the seabed layer, and  $L_2$  is the liquid/elastic interaction boundary between the seawater and the sea bottom.  $\rho_w$  and  $c_w$  are seawater density and seawater sound speed, respectively.  $\rho_b$  is the density of the sea bottom, while  $c_p$  and  $c_s$  are the P-wave speed and S-wave speed in the sea bottom, respectively. The sound source is located on the  $z$ -axis at a depth of  $z_s$ .  $H_1$  and  $H_2$  are the thickness of the seawater layer on the two sides of the simulation model. To simulate the propagation of sound waves in a semi-infinite medium, the perfectly matched layer (PML) is added to the model to absorb the sound waves [22–24].

For the sound pressure  $p(\mathbf{r}, t)$  at coordinate  $\mathbf{r}$  in  $V_w$  of the ideal seawater layer, considering the action of the point sound source, the sound pressure  $p(\mathbf{r}, t)$  in  $V_w$  satisfies the wave equation [5, 25, 26].

$$\nabla^2 [p(\mathbf{r}, t)] = \frac{1}{c_w^2} \frac{\partial^2 [p(\mathbf{r}, t)]}{\partial t^2} - \delta(\mathbf{r} - \mathbf{r}_0). \quad (1)$$

Assuming that  $V_w$  is dispersed into a finite number of units and  $\mathbf{N}$  nodes, the sound pressure  $\mathbf{p}(\mathbf{r}, t)$  at any point in the space can be expressed as

$$\mathbf{p}(\mathbf{r}, t) = \mathbf{N}^T(\mathbf{r})\mathbf{p}'(t), \quad (2)$$

where  $\mathbf{N}(\mathbf{r})$  is the column vector composed of the basis function  $\mathbf{N}_n(r)$  of each node element and  $\mathbf{p}'(t)$  is the column vector composed of sound pressure  $p_n(t)$  on each node,  $n = 1, 2, \dots, N$ .

$L_1$  is assumed to be a flat pressure release boundary.

$$p(t) = 0 \text{ (on } L_1). \quad (3)$$

In the elastic submarine layer  $V_b$ , acoustic wave propagation can be affected not only by P-wave sound velocity but also by S-wave sound velocity, so the form of the governing equation is as follows:

$$(\lambda + \mu)\nabla(\nabla \cdot \mathbf{s}) + \mu\nabla^2 \mathbf{s} - \rho_b \frac{\partial^2 \mathbf{s}}{\partial t^2} + \mathbf{f} = 0, \quad (4)$$

where  $\mathbf{s}(\mathbf{r})$  is the displacement vector on the space coordinate point  $\mathbf{r}$ ;  $\lambda$  and  $\mu$  are Ramet constants;  $\mathbf{f}$  is for volume force. Using finite element method, the discrete form of formula (4) is

$$\mathbf{s}(\mathbf{r}, t) = \mathbf{N}^T(\mathbf{r})\mathbf{s}'(t), \quad (5)$$

where  $\mathbf{N}(\mathbf{r})$  is the column vector composed of the basis function  $\mathbf{N}_n(\mathbf{r})$  of each node element and  $\mathbf{s}'(t)$  is the column vector composed of the displacement  $\mathbf{s}_n(t)$  on each node  $n = 1, 2, \dots, N$ .

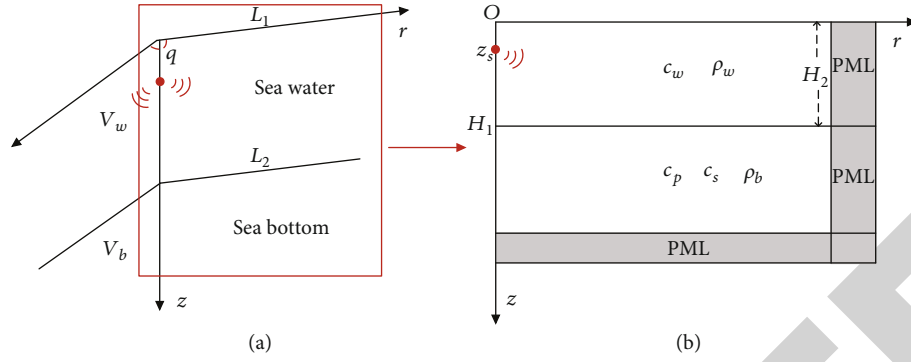


FIGURE 1: The full waveguide model for shallow sea. (a) The waveguide model in three-dimensional cylindrical coordinates; (b) the solution region in the  $(r, z)$  plane.

At the liquid-elastic coupling interface where  $V_w$  is in the seawater layer and  $V_b$  is in the elastic seabed layer, the boundary conditions follow

$$\frac{1}{\rho_w} \mathbf{n} \nabla \mathbf{p}(t) = -\mathbf{n} \frac{\partial^2 \mathbf{s}(t)}{\partial t^2} \quad (\text{on } L_2), \quad (6)$$

where  $\mathbf{n}$  is the unit normal vector of the interface.

Substitute the discrete sound pressure field and displacement field into equation (6). The liquid-elastic coupling equation can be expressed as

$$\begin{bmatrix} \mathbf{K}_s & \mathbf{K}_c \\ 0 & \mathbf{K}_w \end{bmatrix} + j\omega \begin{bmatrix} \mathbf{C}_s & 0 \\ 0 & \mathbf{C}_w \end{bmatrix} - \omega^2 \begin{bmatrix} \mathbf{M}_s & 0 \\ -\rho_0 \mathbf{K}_c^T & \mathbf{M}_w \end{bmatrix} \times \begin{bmatrix} \boldsymbol{\mu}_i \\ \mathbf{p}_i \end{bmatrix} = \begin{bmatrix} \mathbf{F}_{st} \\ \mathbf{F}_{wt} \end{bmatrix}, \quad (7)$$

where  $F_{st}$  and  $F_{wt}$  are the coupled loads of the sea bottom and seawater media, respectively.  $\mathbf{K}_c$  is the coupling stiffness matrix.  $\mathbf{M}_c^T = -\rho_0 \mathbf{K}_c^T$ , where  $\mathbf{M}_c$  is the coupling mass matrix [27].

As shown in Figure 1(b), to simulate the propagation of sound waves in an infinite shallow sea, a PML is added at the boundary during numerical calculation. The PML is highly efficient in truncating the infinite domain with minimal spurious reflections [22–25]. By coupling the physical field, liquid-elastic coupling, and PML equations, sound wave field in the seawater and the sea bottom layers for shallow sea environment can be calculated. Physical field values such as vibration velocity field  $v$  and seabed stress  $\sigma$  can be obtained through the corresponding relationship between these fields to the elastic displacement  $s$ . This study will implement the calculation process on the finite element software COMSOL Multiphysics platform.

### 3. Accuracy Analysis

To assess the accuracy of the proposed FETD, shallow sea model, the sound wave propagation in the full waveguide is calculated and verified using the spectral element method (SEM) [28]. SEM is widely used in seismology for its high

precision and fast calculation speed [29–31]. Recently, some scholars [28] conducted a numerical calculation of shallow-sea sound fields in the time domain using SEM. During the assessment, the model was designed as a horizontal layered structure and nonhorizontal layered structures (uphill and downhill), as shown in Figure 2. The sound velocity in seawater is 1500 m/s; density of seawater is 1000 kg/m<sup>3</sup>; and density of the sea bottom layer is 1500 kg/m<sup>3</sup>. The P-wave velocity and S-wave velocities were 2400 m/s and 1200 m/s, respectively, and their attenuations are both 0.1 dB/λ. The sound source in this study adopts the Ricker wavelet uniformly, and its time-domain equation is formula (8). The sound source was located at 395 m on the  $z$ -axis in the seawater layer, and the central frequency  $f_r$  of sound source is 30 Hz, as shown in Figure 3.

$$r(t) = [1 - 2(\pi f_r t)] \exp[-(\pi f_r t)^2]. \quad (8)$$

In the process of numerical calculation, the mesh size and time step are significant to the accuracy of the solution results. The mesh size  $h$  in this study is set as  $\lambda/6$  to ensure that it is sufficient to resolve a wavelength in the spatial domain. In addition, the CFL condition is an important criterion for judge the stability and convergence of the scheme [32].

$$\text{CFL} = \frac{c\Delta t}{h}, \quad (9)$$

where  $c$  is the speed of sound in the medium and  $\Delta t$  is the solution time step. Generally, when CFL is less than 0.2, the accuracy of the solution results can be guaranteed. Therefore, the solution time step  $\Delta t$  is set as  $T_r/25$  ( $\lambda$  is the wavelength of sound waves, and  $T_r$  is the period of the sound source).

Based on the three simulation conditions in Figure 2, Figure 4 shows the wave field snapshots at different times. It can be seen from Figure 4 that certain types of waves are excited by the sound source in the full waveguide, which is represented by the letters  $a$ – $f$  in the snapshot. Here,  $a_1$  is the direct wave;  $a_2$  is the wave reflected once from the sea surface;  $b$ , Scholte wave;  $c$ , S-wave;  $d$ , P-wave;  $e$ , the side wave associated with the P-wave; and  $f$  is the side wave related to the S-wave. In the single section, wavefronts of

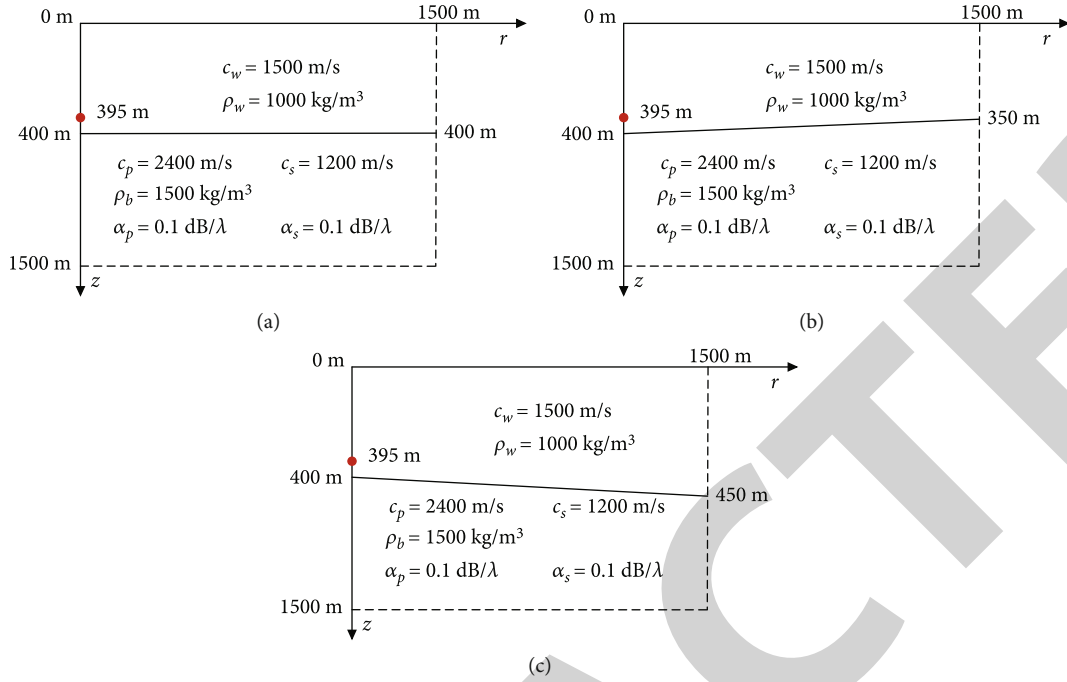


FIGURE 2: Three types of shallow-sea full-waveguide models and their parameters in simulation verification. (a) Horizontal sea bottom. (b) Uphill sea bottom. (c) Downhill sea bottom.

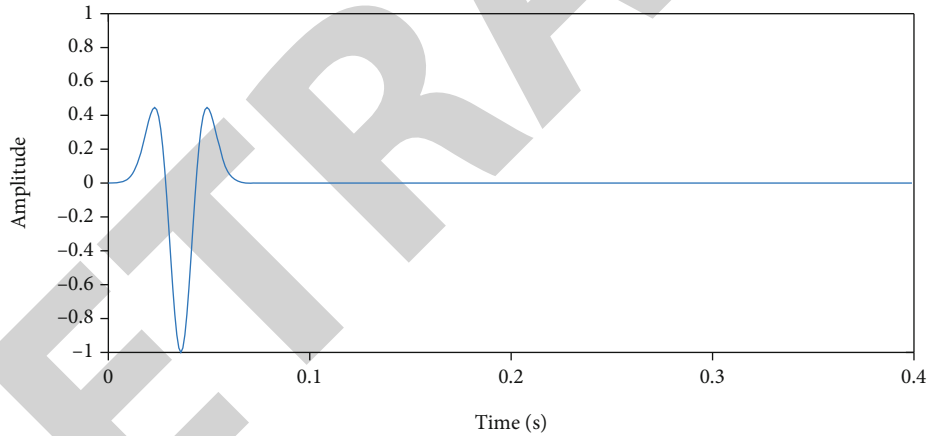


FIGURE 3: The Ricker wavelet emitted by VLF sound source.

$a_1$ ,  $a_2$ ,  $c$ , and  $d$  are circular, while wavefronts of  $e$  and  $f$  are straight. The Scholte wave propagates along the liquid-elastic coupling boundary, and its energy is mainly concentrated near the liquid-solid interface. In addition, it can be seen from Figures 4(b) and 4(c) that the PML added around the model can absorb sound waves well, indicating that the numerical model achieves a good simulation of semi-infinite space.

Figure 5 shows the time-domain waveform comparison of the receiving point (400 m, 380 m) under the three simulation conditions in Figure 2. According to the wave field distribution in Figure 4 and propagation velocity, the wave components can be distinguished at different times, as shown in Figure 5. Although the amplitude of the same wave field components varies under different simulation conditions, the results of the two numerical simulation methods

are in good agreement, thus validating the effectiveness of FETD. However, studies [33] have demonstrated that SEM is not as accurate and fast as the finite element method for solving low-order polynomials. Hence, based on the FETD, the full waveguide sound field model is divided into triangular mesh for solving. The equations of each unit are linked together to obtain an approximate solution for the entire physical field.

#### 4. Simulation and Discussion

After studying the existing literature, it is found that sea-bottom geoaoustic parameters and sea-bottom topographic changes significantly impact the distribution of wave fields; hence, further research is needed in this field of study. The FETD was used to simulate the waveforms for the full



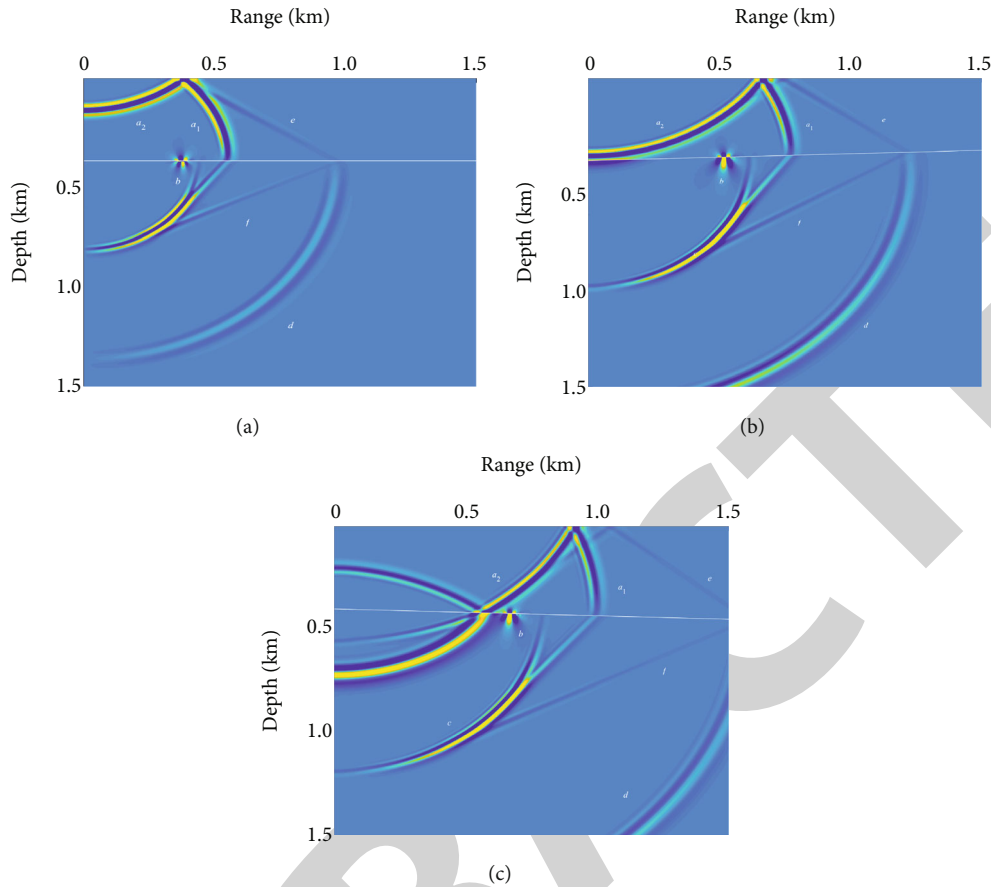


FIGURE 4: Snapshot of wave field in full waveguide. (a) Horizontal sea bottom, 0.4 s. (b) Uphill sea bottom, 0.55 s. (c) Downhill sea bottom, 0.7 s.

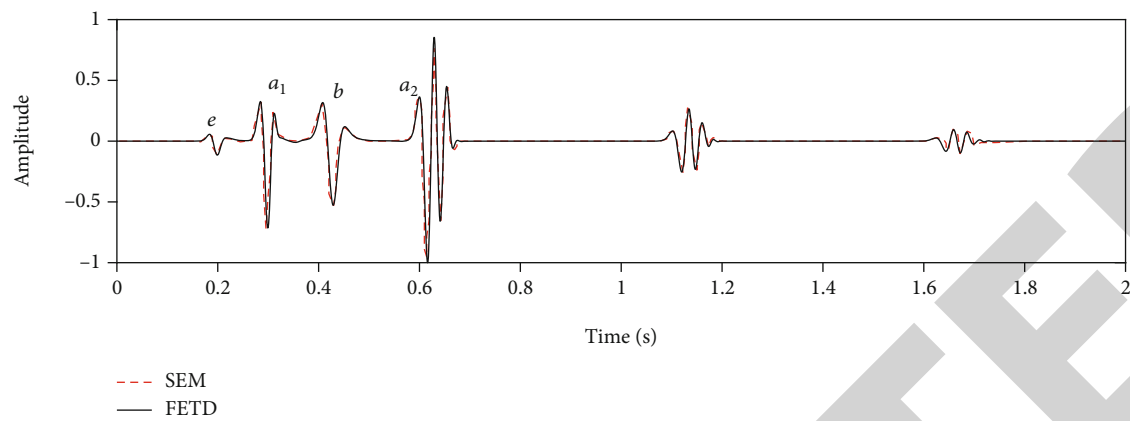
waveguide shallow sea model under different parameters. During the simulation, the sound source was placed at 90 m on the  $z$ -axis in the seawater layer. The source function was a Ricker wavelet with a central frequency of 20 Hz. The depth and length of the seawater layer were 100 m and 6 km, respectively. The acoustic parameters in seawater and sea bottom layers are listed in Table 1.

**4.1. The Effects of Sea-Bottom Geoacoustic Parameters on Low-Frequency Sound Field.** In this section, the effects of the two most common types of sea bottoms: the hard sea bottom and soft sea bottom, based on the FETD on low-frequency sound fields, are discussed. The speed of S-wave velocity in the hard sea bottom is greater than the speed of sound in water, while that in the soft sea bottom is lesser.

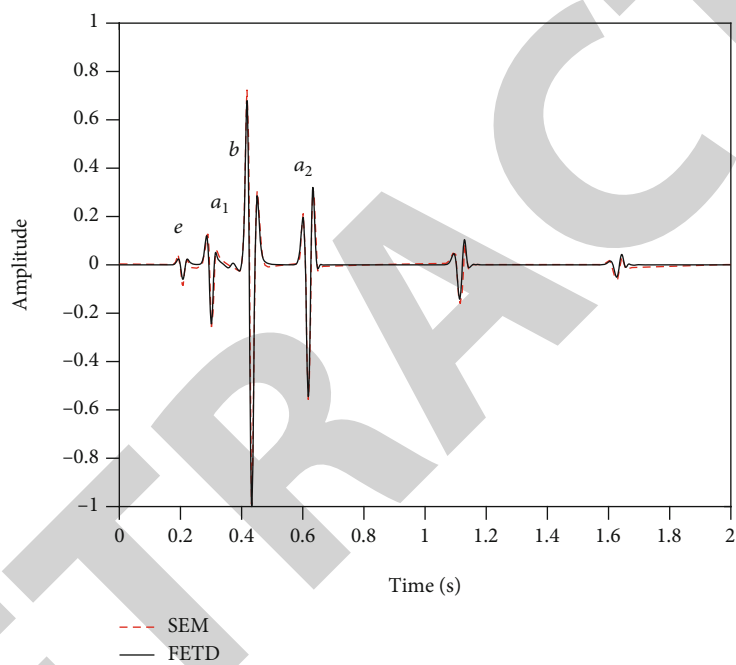
Figure 6 presents the snapshot of the wave field in two full waveguides: one modelled for hard sea bottom and the other for soft sea bottom. As demonstrated in Figure 6, the waves excited by the low-frequency sound source in two full waveguides are represented by  $a$ – $d$ . Among these waves,  $a$  is the sound wave propagated in the seawater layer after repeated reflection from the sea surface to the sea bottom. After it propagates to the far field, the curvature of its wavefront becomes very small. The propagation characteristics are almost lost along the vertical direction, forming wave groups mainly along the horizontal path, usually called nor-

mal mode waves [34]. The letter  $b$  denotes the Scholte wave;  $c$ , the S-waves; and  $d$ , the P-waves. In Figures 6(a) and 6(b), the low-frequency sound field components of the hard sea bottom in the near and far fields are mainly the normal mode waves, Scholte waves, and S-waves. However, the amplitude of the S-wave in the far field is very minimal. Under the soft sea bottom conditions listed in Table 1, the low-frequency sound field components mainly consist of the normal mode waves, Scholte wave, S-wave, and P-wave in the near field (Figure 6(c)), while in the far field (Figure 6(d)), the low-frequency sound field components mainly consist of the normal mode waves and Scholte wave. In the near field (Figure 6(a)), the Scholte wave excited by the VLF sound source in the hard sea bottom has a faster wave speed. Hence, the Scholte waves are mixed with normal mode waves and S-waves and are gradually separated in the far field (Figure 6(b)). In contrast, the Scholte wave in the soft sea bottom has a slower speed and can be clearly distinguished from other sound waves in near and far fields.

To further analyze the propagation characteristics of different wave field components, vertical and horizontal received signals were obtained. Ten receivers placed 50 m underwater and spaced 500 m apart are used to receive the normal mode waves in the seawater layer. Figures 7(a) and 7(b) show the received waveforms in two full waveguides. Figure 8(a) shows the received Scholte waves at ten receivers



(a)



(b)

FIGURE 5: Continued.

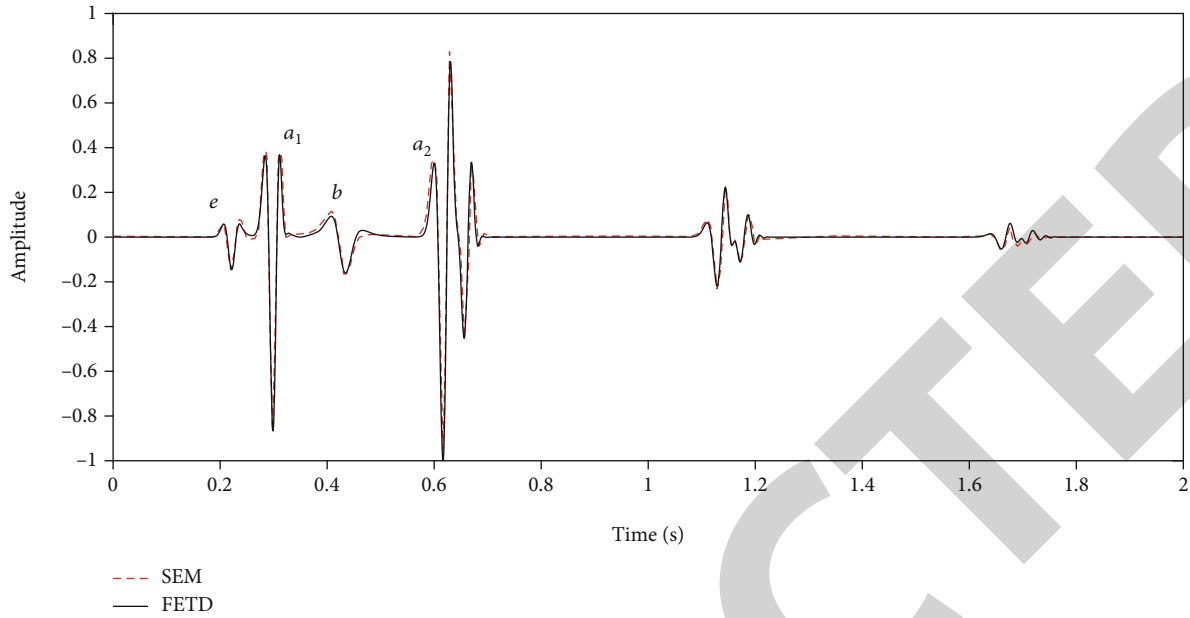


FIGURE 5: Waveforms at the receiving position (400 m, 380 m); FETD (solid line) and SEM (dot line). (a) Horizontal sea bottom. (b) Uphill sea bottom. (c) Downhill sea bottom.

TABLE 1: Parameters for calculation.

Medium	Density ( $\text{g}\cdot\text{cm}^{-3}$ )	P-wave speed ( $\text{km}\cdot\text{s}^{-1}$ )	S-wave speed ( $\text{km}\cdot\text{s}^{-1}$ )
Seawater	1.00	1.50	0.00
Hard sea bottom	1.85	3.40	1.60
Soft sea bottom	1.50	1.80	0.80

placed 100 meters underwater and spaced 250 m apart. Figure 8(b) shows the received Scholte waves and normal mode waves at ten vertical receivers placed 2400 m underwater in the direction of the  $r$ -axis and spaced 10 m apart.

In Figure 8(a), all receivers received two groups of waveforms. The amplitude of wave group 1 gradually attenuates with propagation range, and its group velocity is about 1503 m/s. The amplitude of wave group 2 decreases slowly with propagation range, and its group velocity is about 1360 m/s. In contrast to Figure 7(a), it can be concluded that wave groups 1 and 2 are the normal mode waves and Scholte waves, respectively, in the seawater. Figure 8(b) shows only the normal mode waves (wave group 1). In addition, the attenuation rate of normal mode waves in Figure 8(b) is faster than that in Figure 8(a).

As shown in Figure 8(a), the Scholte waves in both types of sea bottoms can propagate with long range and slow attenuation, but the amplitude of Scholte waves in hard sea bottom is significantly higher than that in soft bottom. In Figure 8(b), the receivers at all depths of the hard sea bottom received the Scholte waves behind the normal mode waves. The amplitude of Scholte waves decreases exponentially from the sea bottom to the sea surface. However, the receivers in the soft sea bottom received Scholte waves near

$t = 3.6$  s, mainly below 60 m, and no obvious Scholte waves were received above 60 m.

Comparing with the calculation results demonstrated in Figures 5–7, it can be concluded that the normal mode waves attenuate faster in the shallow sea with soft sea bottom; hence, the hard sea bottom is more suitable for the long propagation of normal modes waves. In both types of shallow sea environments, the Scholte waves can propagate with slow attenuation over a long range in the horizontal direction; however, the waves have different characteristics in the vertical direction. In the hard sea bottom, the amplitude of the Scholte waves can be received from the sea bottom to the surface, and their amplitude decreases exponentially. The Scholte waves on soft sea bottom are concentrated mainly in the liquid-solid interface, and their amplitude intensity is weaker than that on the hard sea bottom.

According to the wave reflection and refraction on a liquid-solid interface theory [35], the interface wave of the elastic bottom is composed of inhomogeneous P-wave and inhomogeneous S-wave. They can be excited by a low-frequency sound source when the grazing angle is small on the hard sea bottom; hence, it is conducive to the excitation of interface waves. In a soft sea bottom, the speed of an S-wave is less than the speed of sound in water. Even if the grazing angle of the sound source is very small, only the inhomogeneous P-wave exists in an elastic sea bottom. The S-wave can transmit part of the energy to the elastic sea bottom, such that the sound energy is not limited to the bottom interface. Therefore, the soft sea bottom is not conducive to the excitation of interface waves. In addition, when the speed of the S-wave is less than the speed of sound in water, no waveguide normal mode waves can propagate normally in the water, so normal mode waves attenuate faster on the soft sea bottom.



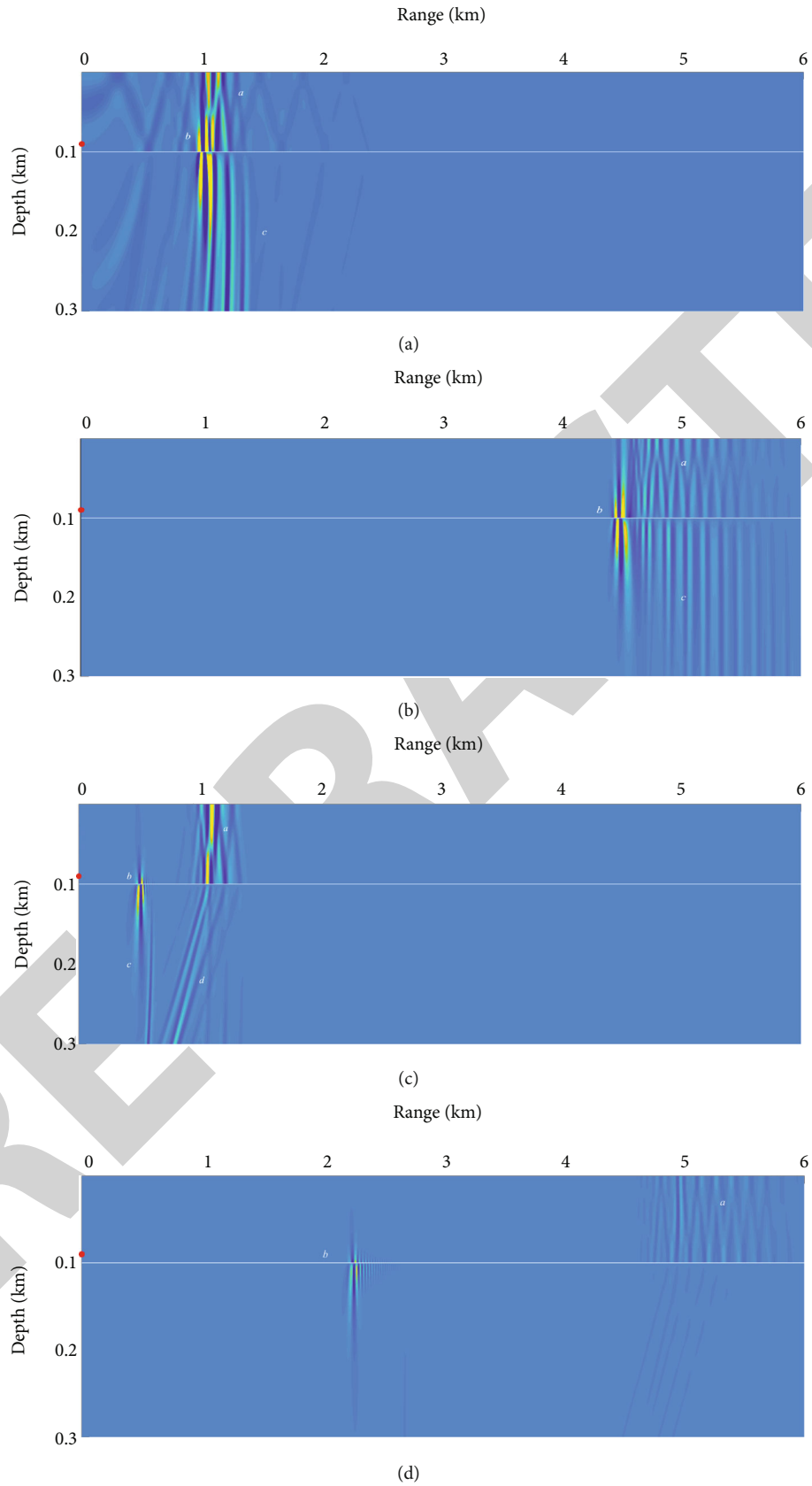


FIGURE 6: Snapshot of wave field in full waveguide. (a) Hard sea bottom, 0.8 s. (b) Hard sea bottom, 3.4 s. (c) Soft sea bottom, 0.8 s. (d) Soft sea bottom, 3.4 s.

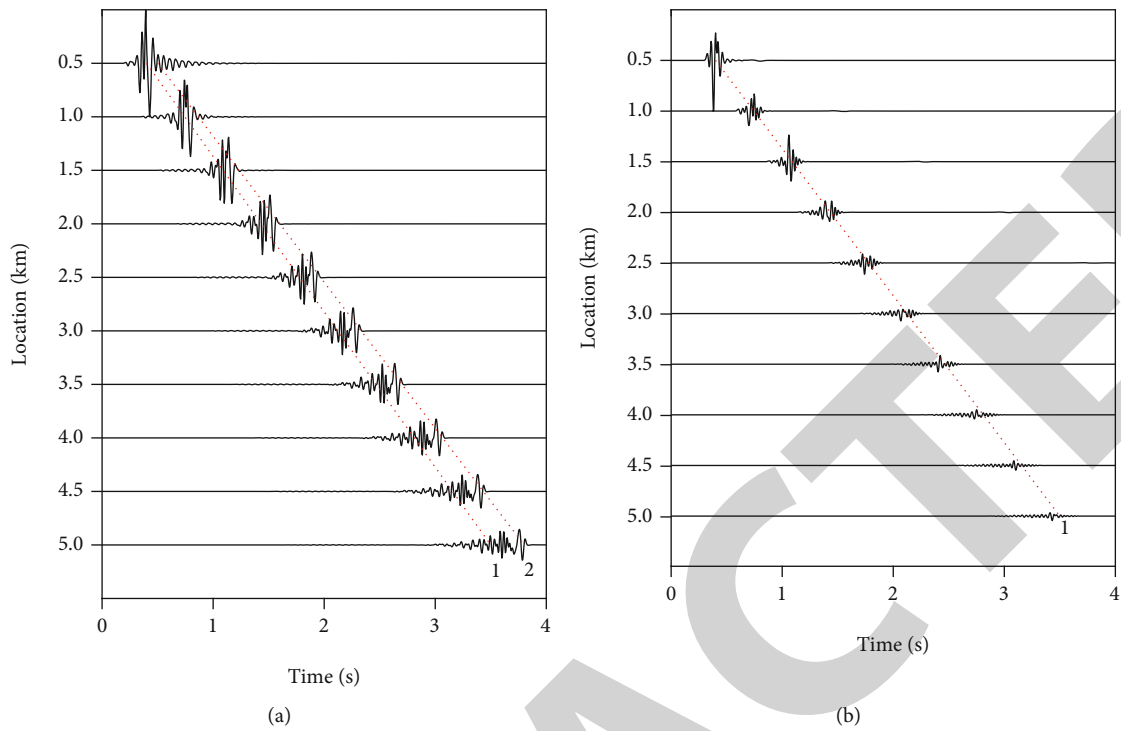


FIGURE 7: Received signals in time domain at different horizontal positions. (a) Hard sea bottom, receiver depth: 50 m. (b) Soft sea bottom, receiver depth: 50 m.

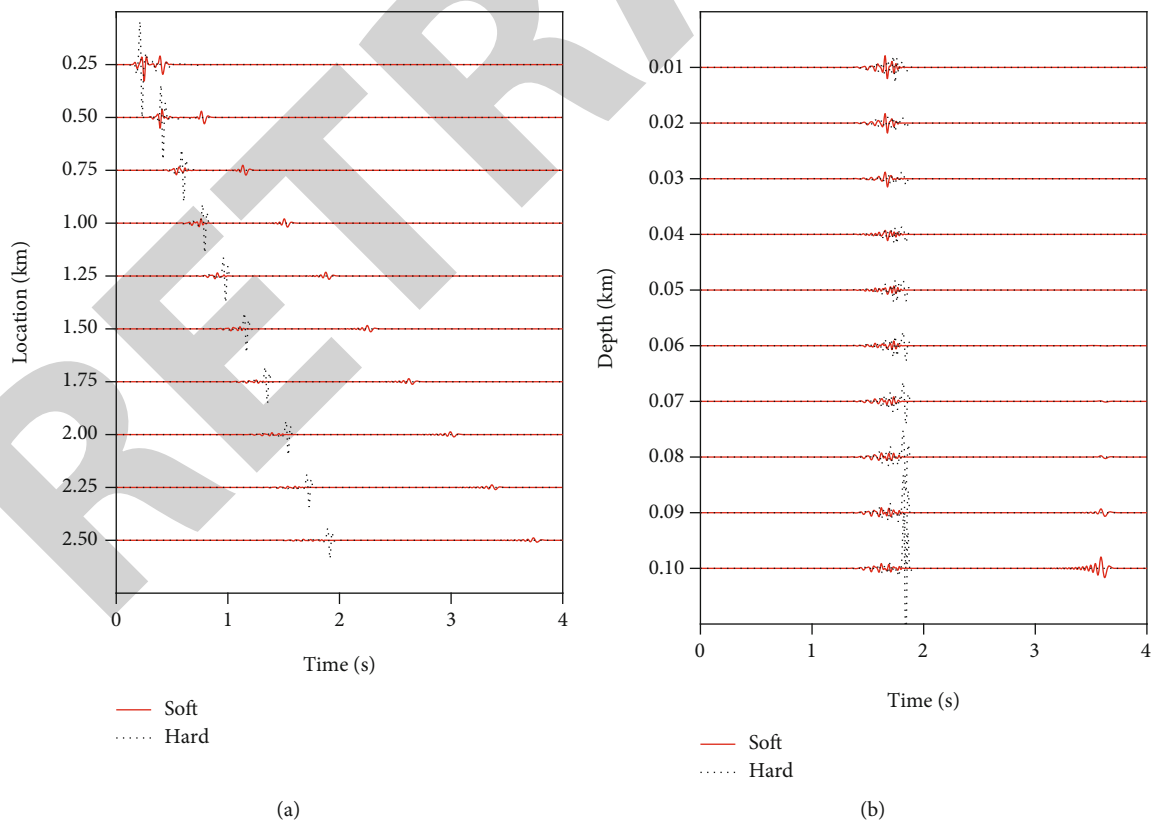


FIGURE 8: Contrast diagram of the received signals in the time domain. (a) Horizontal receiver array, receiver depth: 100 m. (b) Vertical receiver array, receiver position: 2400 m.

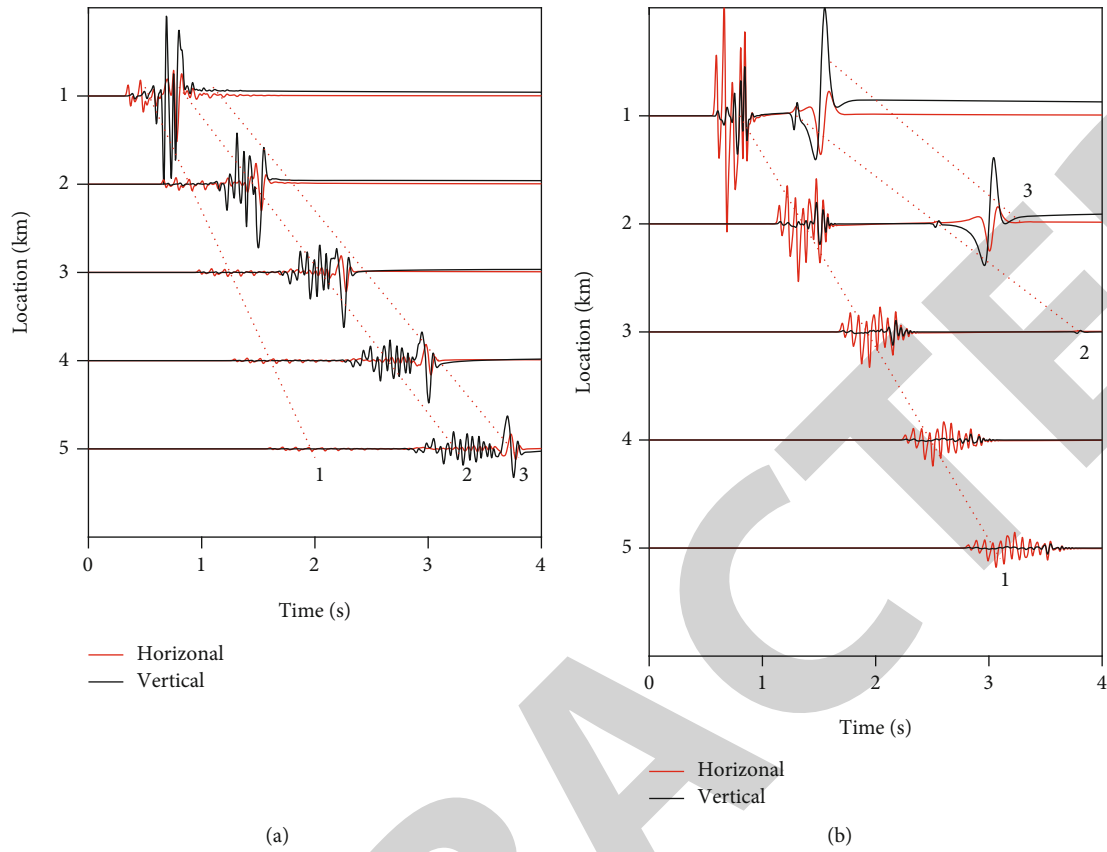


FIGURE 9: Contrast diagram of sea bottom stress. (a) Hard sea bottom, receiver depth: 180 m. (b) Soft sea bottom, receiver depth: 180 m.

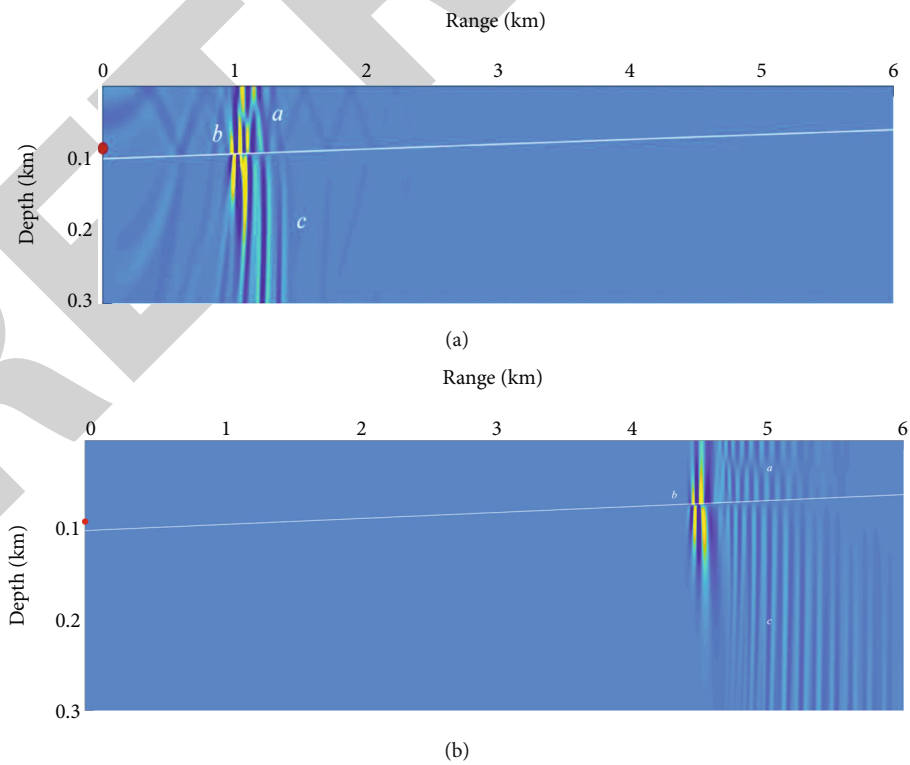


FIGURE 10: Snapshot of wave field in full waveguide. (a) Uphill hard sea bottom, 0.8 s. (b) Uphill hard sea bottom, 3.4 s.

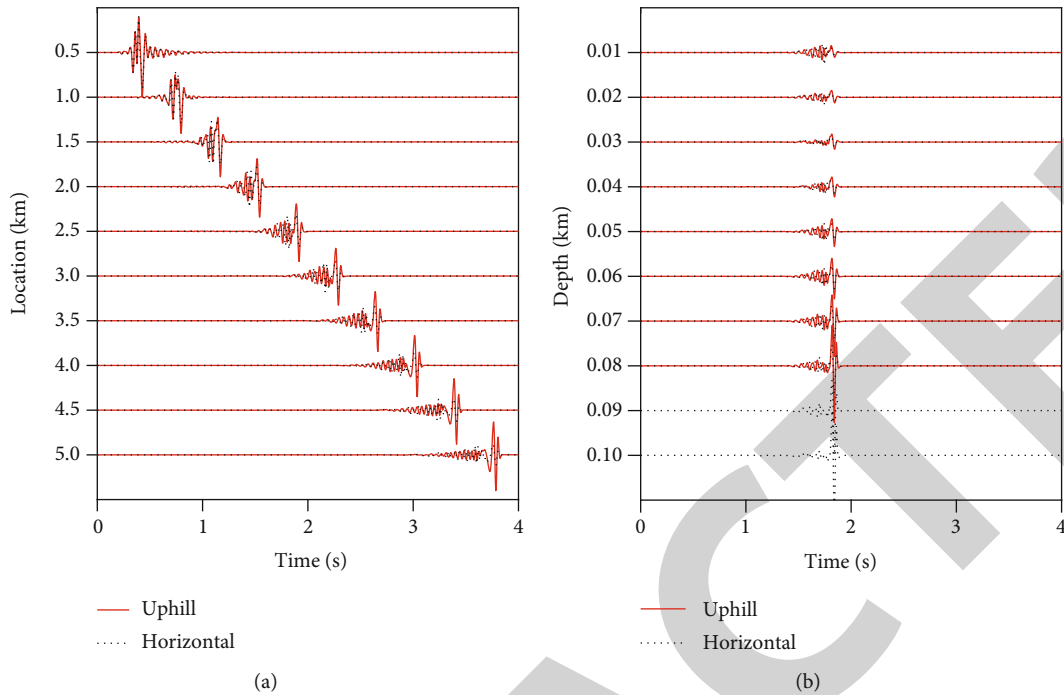


FIGURE 11: Contrast diagram of the received signal in time domain. (a) Horizontal receiver array, receiver depth: 50 m. (b) Vertical receiving array, receiver position: 2400 m.

To study the propagation characteristics of these waves in the sea bottom, five receivers are placed at 180 m underwater, within 500 m–5000 m, and 1000 m apart. Based on the propagation velocity, wave groups 1, 2, and 3 were identified as the submarine P-wave, submarine S-wave, and Scholte wave, respectively. In hard sea bottom (Figure 9(a)), the amplitude of the P-wave with horizontal stress is much smaller than that of the S-wave with vertical stress. However, in soft sea bottom (Figure 9(b)), the amplitude of the P-wave with horizontal stress is much higher than that of the S-wave with vertical stress. The vertical stress of the Scholte wave propagating in both sea bottoms is greater than its horizontal stress.

**4.2. The Effects of Sea-Bottom Topographies on Low-Frequency Sound Field.** In this section, the influence of the inclined sea bottom (uphill and downhill) on the full waveguide propagation characteristics of low-frequency sound waves is discussed, along with the corresponding theoretical explanations. In the uphill sea bottom,  $H_1$  and  $H_2$  are 100 m and 60 m; the slope angle is  $0.38^\circ$ .  $H_1$  and  $H_2$  in the downhill sea bottom are 100 and 140 m; the slope angle is  $0.38^\circ$ . The model was simulated for a hard sea bottom topography, with the same geoacoustic parameters as shown in Figures 6(a) and 6(b).

The receiver signals in Figures 10(a) and 10(b) are consistent with those in Figures 7 and 8(b), respectively. In contrast, the uphill sea bottom has a depth of 80 m at the horizontal level of 2400 m; hence, no signal is received from 80 m to 100 m in Figure 11(b). As shown in Figure 11(a), the normal mode waves in water attenuate gradually with propagation range on both uphill and horizontal sea bottom topographies. However, the normal mode waves on the

uphill sea bottom topography attenuate faster than those in the horizontal sea bottom, indicating a faster leakage rate to the sea bottom. The Scholte waves excited by VLF sound source on horizontal sea bottom have little change with the propagation range. In contrast, the amplitude of Scholte waves in uphill sea bottom increases with propagation range. In Figure 11(b), both types of sea bottoms can receive Scholte waves from the sea surface to the sea bottom, and the amplitude shows the exponential increase trend from the sea surface to the sea floor. However, at any given receiver depth, the amplitude of Scholte waves received on the uphill sea bottom is stronger than that on the horizontal sea bottom.

The positions of horizontal and vertical received signals in Figure 12 are consistent with those in Figure 11. In Figure 12, as the propagation range increases, the normal mode waves on the downhill sea bottom attenuate more slowly than on the horizontal sea bottom, indicating a slower leakage rate to the sea bottom. In both horizontal and vertical directions, the Scholte waves excited by VLF sound sources on the downhill sea bottom are weaker than those on the horizontal sea bottom, which is the opposite of the Scholte waves on the uphill sea bottom (Figure 11).

Comparing the calculation results in Figures 10–13, the attenuation of normal mode waves is the fastest on the uphill sea bottom. Hence, the uphill sea bottom is not conducive to the long-range propagation of normal mode waves, while the downhill sea bottom is conducive to the long-range propagation of normal mode waves. At the same depth, the amplitude of excited Scholte waves is the strongest on the uphill sea bottom, followed by the horizontal sea bottom

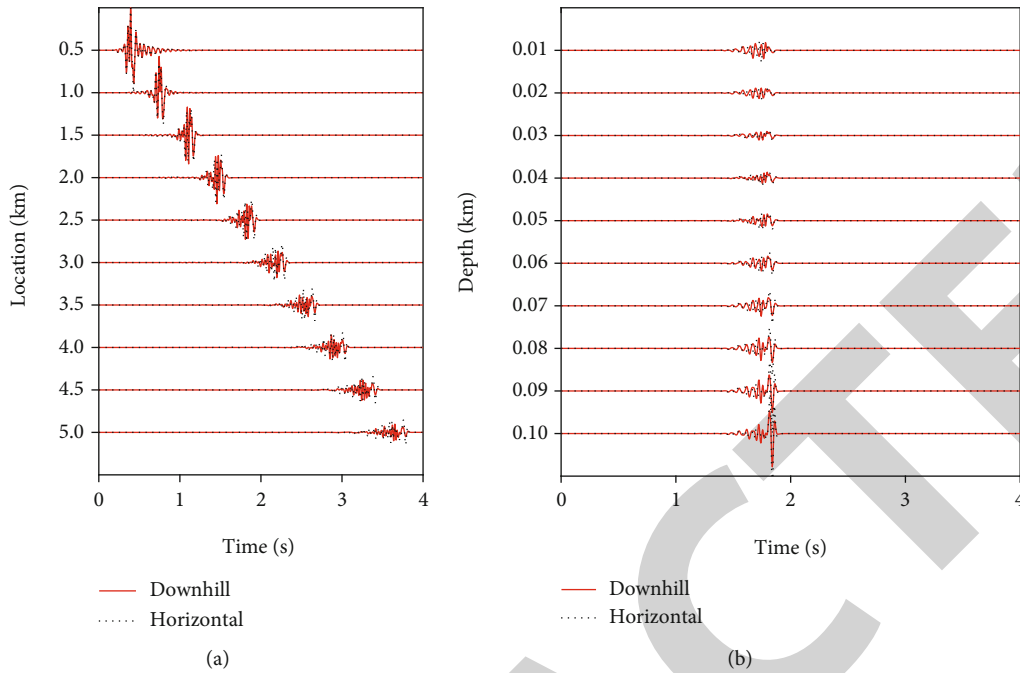


FIGURE 12: Contrast diagram of the received signal in time domain. (a) Horizontal receiving array, receiver depth: 50 m. (b) Vertical receiving array, receiver position: 2400 m.

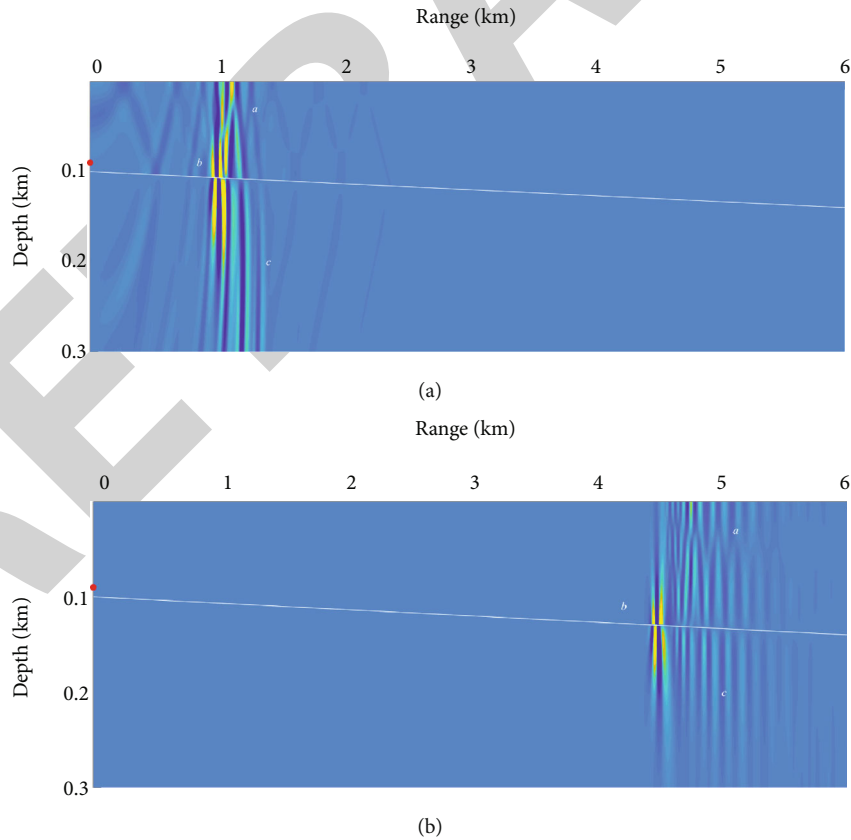


FIGURE 13: Snapshot of wave field in full waveguide. (a) Downhill hard sea bottom, 0.8 s. (b) Downhill hard sea bottom, 3.4 s.

and, finally, the downhill sea bottom. Hence, the uphill sea bottom is favorable for Scholte wave reception; the downhill sea bottom is not conducive to Scholte wave reception.

To explain the sound propagation characteristics of inclined sea bottom (Figures 11 and 12), a theoretical interpretation is given based on the ray track distribution of

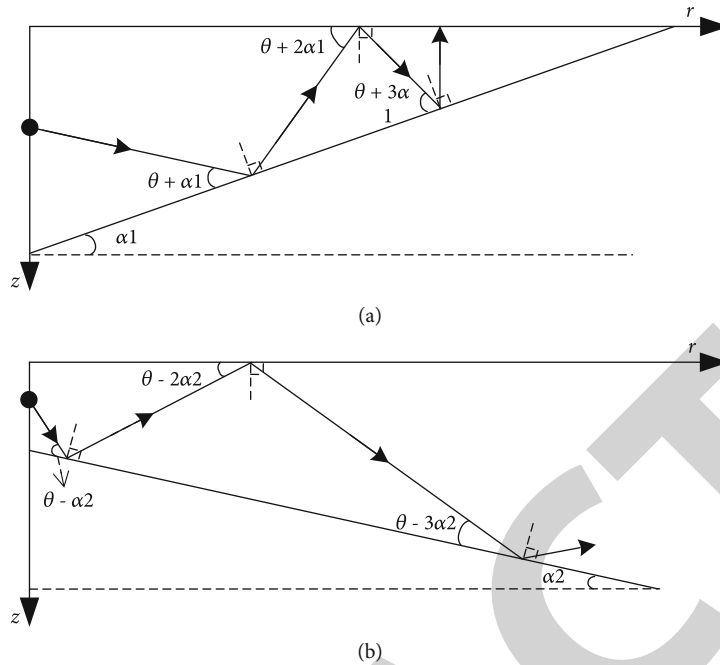


FIGURE 14: Distribution of the ray tracing in inclined sea bottom topographies. (a) Uphill sea bottom. (b) Downhill sea bottom.

acoustic signals. In the uphill sea bottom of the shallow sea (Figure 14(a)), normal mode waves incident at grazing angle  $\theta + \alpha_1$ , where  $\alpha_1$  is the slope angle, are coupled to normal mode waves incident at grazing angle  $\theta + 3\alpha_1$  after a bottom-surface reflection. Hence, the lower-order normal mode waves propagating at the small grazing angle will gradually be coupled to the higher-order normal mode waves propagating at the large grazing angle. The increase of high-order normal modes leads to more acoustic energy leaking into the sea bottom, which explains the faster attenuation of normal mode waves in the uphill sea bottom than in the horizontal sea bottom in Figures 10 and 11.

In the downhill sea bottom of the shallow sea (Figure 14(b)), the normal mode waves incident at grazing angle  $\theta - \alpha_1$  are coupled to normal modes incident at grazing angle  $\theta - 3\alpha_1$  after experiencing a bottom-surface reflection, which is the opposite of the situation in the uphill bottom shown in Figure 14(a). Hence, the higher-order normal mode waves propagating at a large grazing angle will gradually be coupled to the lower-order normal mode waves propagating at a small grazing angle. The increase of the lower-order normal mode waves will weaken the acoustic energy leaks into the sea bottom. Figures 12 and 13 demonstrate that the attenuation of normal mode waves on the downhill sea bottom is weaker than that on the horizontal sea bottom.

Scholte waves propagate over a long range with slow attenuation along the liquid-solid interface. Scholte waves rise or fall with the topography when the sea bottom rises or falls. Meanwhile, the Scholte waves are the strongest at the liquid-solid interface and attenuate exponentially toward the sea surface. Hence, the amplitude of the Scholte wave is the strongest in the uphill sea bottom at the same depth, followed by the horizontal sea bottom, and the weakest in the downhill sea bottom.

## 5. Conclusions

The study has proposed a full waveguide model based on FETD for sound propagation in the shallow sea. In the study, the time-domain waveform of the signal is taken as the research object, and the effects of different sea-bottom geoacoustic parameters and topographies on the low-frequency sound propagation characteristics were discussed and analyzed. The research results can provide further improvement direction for developing low-frequency sound transducers and related equipment in the shallow seas. The specific conclusions of this study are as follows.

In the near field, the low-frequency sound field components in soft sea bottom are mainly normal mode waves, Scholte wave, S-wave, and P-wave, while those in hard sea bottom do not include P-wave. In the far field, the low-frequency sound components of soft and hard sea bottom are mainly simple normal mode waves and Scholte waves.

In contrast to the soft sea bottom, the hard sea bottom is more suitable for the long-range propagation of normal mode waves and the excitation of Scholte wave. Scholte waves excited by low-frequency sound sources on the hard sea bottom can be received from the sea bottom to the surface, while Scholte waves excited by soft sea bottom are mainly concentrated on the liquid-solid interface. In addition, the hard sea bottom mainly vibrates in the vertical direction, while the soft sea bottom mainly vibrates in the horizontal direction. The vertical stress of the Scholte wave is dominant in both sea bottoms.

Compared with the horizontal sea bottom, the uphill sea bottom strengthens the leakage effect of the acoustic energy in the seawater to the sea bottom. On the contrary, the downhill sea bottom will confine more acoustic energy in the seawater layer. Scholte waves are the strongest at the



liquid-solid interface and attenuate exponentially toward the sea surface. Hence, when the topography of the sea bottom rises or falls, the amplitude of the Scholte wave at the same depth is the strongest in the uphill sea bottom, weaker in the horizontal sea bottom, and the weakest in the downhill sea bottom.

## Data Availability

Data are available on request from the authors.

## Conflicts of Interest

The authors declare that they have no conflicts of interest.

## Acknowledgments

Thanks are due to Professor Shengchun Piao's research group from the College of Underwater Acoustic Engineering, Harbin Engineering University, for providing finite element software support for writing this paper. This research project was supported by the Science Foundation of Donghai Laboratory (Grant No. DH-2022KF01018), the General Project of the Education Department of Zhejiang Province (Y202147766), the University Student Science and Technology Innovation Activity Plan of Zhejiang Province (2022R411C050, 2022R411C052), and the Open Fund Project of the Key Laboratory of Marine Environmental Information Technology, Ministry of Natural Resources of the People's Republic of China.

## References

- [1] I. Seo, S. Kim, Y. Ryu, J. Park, and D. S. Han, "Underwater moving target classification using multilayer processing of active sonar system," *Applied Sciences*, vol. 9, no. 21, p. 4617, 2019.
- [2] S. Wu, Z. Li, J. Qin, M. Wang, and W. Li, "The effects of sound speed profile to the convergence zone in deep water," *Journal of Marine Science and Engineering*, vol. 10, no. 3, p. 424, 2022.
- [3] J. Li, D. Shang, J. Liu, and C. Zhang, "Sound scattering from targets in shallow water by finite element method combined with normal-mode method," *The Journal of the Acoustical Society of America*, vol. 145, no. 3, pp. 1692–1692, 2019.
- [4] C. C. Roa and G. V. Frisk, "Three-dimensional inversion technique in ocean and seabed acoustics using the parabolic equation method," *The Journal of the Acoustical Society of America*, vol. 138, no. 3, pp. 1928–1928, 2015.
- [5] F. B. Jensen, W. A. Kuperman, M. B. Porter, and H. Schmidt, *Computational Ocean Acoustics*, Springer, New York, New York, 2011.
- [6] M. D. Collins, "A single-scattering correction for the seismo-acoustic parabolic equation," *The Journal of the Acoustical Society of America*, vol. 131, no. 4, pp. 2638–2642, 2012.
- [7] N. Li, M. Zhang, and B. Gao, "Horizontal correlation of long-range bottom reverberation in shallow sloping seabed," *Journal of Marine Science and Engineering*, vol. 9, no. 4, p. 414, 2021.
- [8] W. Y. Luo, X. L. Yu, X. F. Yang, and R. H. Zhang, "Analytical solution based on the wavenumber integration method for the acoustic field in a Pekeris waveguide," *Chinese Physics B*, vol. 25, no. 4, article 044302, 2016.
- [9] N. Li, H. Zhu, X. Wang, R. Xiao, Y. Xue, and G. Zheng, "Characteristics of very low frequency sound propagation in full waveguides of shallow water," *Sensors*, vol. 21, no. 1, p. 192, 2021.
- [10] M. Liang, L. Wang, G. Yu, Y. Ren, and L. Peng, "Study on a detection technique for Scholte waves at the seafloor," *Sensors*, vol. 22, no. 14, p. 5344, 2022.
- [11] T. Tsuji, T. A. Johansen, B. O. Ruud, T. Ikeda, and T. Matsuoka, "Surface-wave analysis for identifying unfrozen zones in subglacial sediments," *Geophysics*, vol. 77, 2012.
- [12] J. Zhu, J. S. Popovics, and F. Schubert, "Leaky Rayleigh and Scholte waves at the fluid–solid interface subjected to transient point loading," *The Journal of the Acoustical Society of America*, vol. 116, no. 4, pp. 2101–2110, 2004.
- [13] E. Lamkanfi, N. F. Declercq, W. Van Paepegem, and J. Degrieck, "Scholte-Stoneley waves on an immersed solid dihedral: generation, propagation and scattering effects," *Ultrasonics*, vol. 54, no. 6, pp. 1685–1691, 2014.
- [14] N. Favretto-Anrès and G. Rabau, "Excitation of the Stoneley–Scholte wave at the boundary between an ideal fluid and a viscoelastic solid," *Journal of Sound and Vibration*, vol. 203, no. 2, pp. 193–208, 1997.
- [15] L. R. F. Rose, P. Blanloeuil, M. Veidt, and C. H. Wang, "Analytical and numerical modelling of non-collinear wave mixing at a contact interface," *Journal of Sound and Vibration*, vol. 468, article 115078, 2020.
- [16] O. A. Godin, "Shear waves and sound attenuation in underwater waveguides," *The Journal of the Acoustical Society of America*, vol. 149, no. 5, pp. 3586–3598, 2021.
- [17] A. V. Grayver, "Parallel three-dimensional magnetotelluric inversion using adaptive finite-element method. Part I: theory and synthetic study," *Geophysical Journal International*, vol. 202, no. 1, pp. 584–603, 2015.
- [18] H. Li, M. Zhao, and X. Du, "Accurate H-shaped absorbing boundary condition in frequency domain for scalar wave propagation in layered half-space," *International Journal for Numerical Methods in Engineering*, vol. 121, no. 19, pp. 4268–4291, 2020.
- [19] A. T. Abawi, "Finite element and boundary methods in structural acoustics and vibration," *The Journal of the Acoustical Society of America*, vol. 141, no. 6, pp. 4300–4300, 2017.
- [20] Z. Ren, T. Kalscheuer, S. Greenhalgh, and H. Maurer, "A finite-element-based domain-decomposition approach for plane wave 3D electromagnetic modeling," *Geophysics*, vol. 79, no. 6, pp. E255–E268, 2014.
- [21] S. E. Yang, *Theory of Underwater Sound Propagation*, Harbin Engineering University Press, Harbin, 2009.
- [22] C. X. Xu, H. G. Zhang, S. C. Piao, S. E. Yang, S. Sun, and J. Tang, "Perfectly matched layer for an elastic parabolic equation model in ocean acoustics," *Journal of Ocean University of China*, vol. 16, no. 1, pp. 57–64, 2017.
- [23] M. Zhuang, Q. Zhan, J. Zhou, Z. Guo, N. Liu, and Q. H. Liu, "A simple implementation of PML for second-order elastic wave equations," *Computer Physics Communications*, vol. 246, article 106867, 2020.
- [24] J. G. Zhao and R. Q. Shi, "Perfectly matched layer-absorbing boundary condition for finite-element time-domain modeling of elastic wave equations," *Applied Geophysics*, vol. 10, no. 3, pp. 323–336, 2013.

- [25] B. Wang, Z. Kuo, T. Guo, L. He, and X. L. Zhang, "Acoustic reflection well logging modeling using the frequency-domain finite-element method with a hybrid PML," *Applied Geophysics*, vol. 15, no. 1, pp. 35–45, 2018.
- [26] H. Liu, B. Wang, G. Tao, K. Zhang, and W. Z. Yue, "Study on the simulation of acoustic logging measurements in horizontal and deviated wells," *Applied Geophysics*, vol. 14, no. 3, pp. 337–350, 2017.
- [27] S. Marburg and B. Nolte, *Computational Acoustics of Noise Propagation in Fluids: Finite and Boundary Element Methods*, Springer, Berlin, 2008.
- [28] Y. Dong, S. C. Piao, and H. G. Zhang, "Application of spectral element method in marine sound propagation. C," in *Proceedings of 2016 Western China Acoustic Academic Exchange Conference*, pp. 100–102, Chengdu, Sichuan Province, China, 2016.
- [29] D. Borisov, R. Modrak, F. Gao, and J. Tromp, "3D elastic full-waveform inversion of surface waves in the presence of irregular topography using an envelope-based misfit function," *Geophysics*, vol. 83, no. 1, pp. R1–R11, 2018.
- [30] X. Huang, C. Yin, C. G. Farquharson et al., "Spectral-element method with arbitrary hexahedron meshes for time-domain 3D airborne electromagnetic forward modeling," *Geophysics*, vol. 84, no. 1, pp. E37–E46, 2019.
- [31] A. Bottero, P. Cristini, D. Komatitsch, and M. Asch, "An axisymmetric time-domain spectral-element method for full-wave simulations: application to ocean acoustics," *The Journal of the Acoustical Society of America*, vol. 140, no. 5, pp. 3520–3530, 2016.
- [32] C. Ogawa, K. Okubo, and T. Tsuchiya, "Evaluation of dependence on calculation parameters in interface settings for finite-difference time-domain analyses of acoustic fields," *The Journal of the Acoustical Society of America*, vol. 140, no. 4, pp. 3251–3251, 2016.
- [33] Y. S. Liu, J. W. Teng, X. Si, and X. Y. Ma, "A comparative study of spectral element method and finite element method in seismic wave field simulation," in *Proceedings of the 22nd Conference of Chinese Geophysics*, pp. 858–860, Chengdu, Sichuan Province, China, 2013.
- [34] Z. H. Lu, Z. H. Zhang, and J. N. Gu, "Analysis on the synthetic seismograms of seismic wave caused by low frequency sound source in shallow sea with porous seabed," *Journal of Computational Acoustics*, vol. 26, no. 4, article 1850001, 2018.
- [35] Z. Y. He and Y. F. Zhao, *Theoretical Basis of Acoustics*, National Defense Industry Press, Beijing, 1966.